Multi-fidelity vortex simulations of rotor flows: Validation against detailed wake measurements

Néstor Ramos-García, Aliza Abraham, Thomas Leweke, Jens Nørkær Sørensen

▶ To cite this version:

Néstor Ramos-García, Aliza Abraham, Thomas Leweke, Jens Nørkær Sørensen. Multi-fidelity vortex simulations of rotor flows: Validation against detailed wake measurements. Computers and Fluids, 2023, 255, pp.105790. 10.1016/j.compfluid.2023.105790 . hal-04281252

HAL Id: hal-04281252
https://hal.science/hal-04281252v1

Submitted on 12 Nov 2023

Graphical Abstract

Multi-fidelity vortex simulations of rotor flows: validation against detailed wake measurements

Néstor Ramos-García, Aliza Abraham,
Thomas Leweke, Jens Nørkær Sørensen

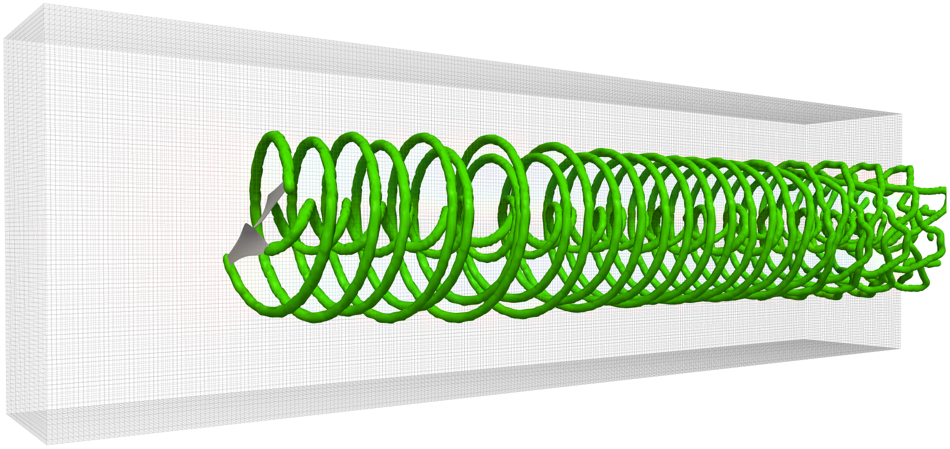

Highlights

Multi-fidelity vortex simulations of rotor flows: validation against detailed wake measurements

Néstor Ramos-García, Aliza Abraham,
Thomas Leweke, Jens Nørkær Sørensen

- Simulation of rotor wakes with two flow models based on vortex solver MIRAS (DTU)
- Validation against experimental results for a two-bladed rotor in water
- New high-resolution PIV measurements accurately resolve the tip vortex core structure
- Models are capable of predicting wake instability resulting from rotor asymmetry

Multi-fidelity vortex simulations of rotor flows: validation against detailed wake measurements

Néstor Ramos-García[a], Aliza Abraham[b],
Thomas Leweke[b], Jens Nørkær Sørensen[a]

[a]*Department of Wind and Energy Systems, Technical University of Denmark, Lyngby, 2800, Denmark*
[b]*IRPHE, Aix-Marseille University, CNRS, Centrale Marseille, Marseille, 13384, France*

Abstract

Two flow models with different fidelity of the DTU vortex solver **MIRAS** have been used to simulate the wake generated by a model wind turbine with various levels of asymmetry. Predictions are validated against experimental Particle Image Velocimetry measurements and dye visualizations. The experiments were conducted in a recirculating free-surface water channel with an immersed two-bladed rotor mounted on a shaft. The blades were designed to approximate a Joukowsky rotor. A detailed comparison between the measurements and the simulations is first performed for an unperturbed baseline case at different tip speed ratios. The analysis consists of a tip vortex characterization, including the vortex core profile, and a comparison of the instantaneous and mean velocity and vorticity fields, along with the mean wake profile at different downstream locations. Overall, good agreement is obtained between measurements and simulations, especially with the higher-fidelity particle-mesh model, which is capable of very closely predicting many of the flow features observed in the experiments. Rotor asymmetry triggers a vortex instability, commonly known as leapfrogging, which accelerates the breakdown of tip vortices, enhancing the mixing of wake structures and promoting a faster wake recovery. The prediction accuracy of this instability by the solvers is analyzed for different tip speed ratios and perturbation amplitudes. This work aims at setting the groundwork for future flow instability studies with the **MIRAS** solver.

Email address: `nerga@dtu.dk` (Néstor Ramos-García)

Preprint submitted to Computers & Fluids *November 23, 2022*

Keywords: Vortex methods, Particle-Image Velocimetry, Rotor wake, Helical vortices

---

1. Introduction

Most renewable energy sources, including wind energy, require large areas and therefore have relatively low power density compared to conventional energy technologies, such as gas. Additionally, the energy extracted in contemporary wind farms is limited by the interaction between the wind turbines, the wind farm, and the atmosphere [1, 2]. Wind turbines generate wakes, with regions of slower wind speed and turbulent air, including coherent vortices released from the blades, nacelle, and support tower. As described by Sørensen [3], if a turbine in a wind farm is operating within the wake of an upstream turbine, the fatigue loading that it experiences is more severe than if the vortices have broken down by instability. In addition, it has less power available, leading to significant energy production losses [4]. Accelerating the wake recovery by promoting the energy cascade from larger vortex structures to smaller scales can improve the efficiency of harvesting energy from the wind.

The wake contribution to increased fatigue loads of downstream turbines and its detrimental impact on the overall wind farm efficiency makes wake control an active research focus area, known to be key for the development of more efficient wind farms. One example of such control can be the use of wake steering to deflect the wake away from downstream machines. Along these lines, Gebraad et al. [5] employed a yaw-based control to obtain an increased farm power and annual energy production, while Hulsman et al. [6] obtained a fatigue load reduction, but at cost of a lower power production.

A deeper knowledge of how the different vortex elements that form the wake interact, e.g. the pairing of helical tip vortices and their transition to an unstable wake, can have an strong impact on the energy production of such enormous engineering systems. An improvement can be achieved by promoting a faster breakdown of the wake, which can be forced by pre-designed perturbations of the vortex system. Such perturbations can be aimed to amplify intrinsic wake vortex instability modes, like the mutual-inductance mode, which appears between consecutive turns of the helix system [7]. Better understanding of the different physical phenomena that occur in the wake, as well as the continuous development of numerical capabilities to accurately model such phenomena, are essential for the future development of the wind energy sector, especially in the planning of new large wind farms [8].

The theoretical background for understanding helical vortex systems was first established by Levy et al. [9] with an analysis of the inviscid linear stability of a filament. This was further developed by Widnall [10], who considered vortices with a viscous core and proved the existence of three different instability mechanisms: short-wave, long-wave and mutual inductance instabilities. The latter one appears when the tip speed ratio increases, the pitch of the helix decreases, and consecutive helix turns start to interact directly. Subsequently, Leishman [11] and Bhagwat et al. [12] further advanced the theoretical understanding of the helical wake stability with focus on the vortex ring state of helicopter rotors, using free-wake vortex methods. More recently, Okulov and Sørensen [13] found that the classical rotor model proposed by Joukowsky in the early 20th century [14], which assumes a constant blade circulation and a vortex system consisting only of tip and root vortices, is unconditionally unstable.

Multiple investigations involving the aerodynamics of horizontal-axis wind turbine wakes have been carried out during the last decades [15], both numerically and experimentally, with one of the focus areas being the wake decay and its effect on downstream machines. In the numerical realm, the stability of wind turbine wakes has been investigated by a number of researchers. Walther et al. [16] investigated the instability of helical vortices using direct numerical simulations of particle vortex methods. An initial good agreement was found with inviscid theory, but simulations predicted a breakdown of the helical vortex system due to the overlapping of the root vortex cores linked to their growth under viscous diffusion. Ivanell et al. [17] performed a numerical study of the stability properties of the tip vortices generated by three-bladed wind turbine rotors, employing a numerical model based on Large-Eddy Simulation (LES) of the Navier-Stokes equations in combination with an actuator line modelling in a one-third domain with periodic boundary conditions. In their study, the vortex spiral was perturbed by adding a small time dependent body force near the tip of the blade, which was set to oscillate following a prescribed sinusoidal function. This study provided numerical evidence of the relation between the inflow turbulence level and the wake breakdown location, pointing out the need for new experiments to further validate this relation. A few years later Sarmast et al. [18] employed the same flow solver, in this case with a full domain, to further analyse the stability properties of the wake, concluding that the full geometry disturbed randomly leads to a new set of unstable modes. They found that the amplification of specific waves along the wake spiral is responsible for triggering the mutual-inductance instability, which was identified as the main cause of wake destabilization and vortex breakdown. Ivanell et al. [19] performed one of the first detailed validations, comparing their numerical simulations with the water channel experiments of Quaranta et al. [20] for a single-bladed rotor. After a small calibration of the blade pitch due to an offset with respect to experiments, a good agreement was obtained regarding the evolution of the integral helix parameters, such as tip vortex circulation and center location.

Experimental work helps to validate and improve numerical models by shedding light on the complex physics of the fluid mechanical problem. Working on propeller wakes, Felli et al. [21] studied the evolution of tip and hub vortices, focusing on the effect of the number of blades and the distance between helices on the onset of instability. Nemes et al. [7] investigated the pairing of helical vortices measured behind a model two-bladed wind turbine, highlighting the importance of the mutual-inductance instability. Leweke's research group has studied for several years the stability of tip vortex systems created by rotor blades. Quaranta et al. [20] investigated the stability of a single helical vortex filament shed from a single-bladed rotor, identifying the geometry and growth rate of various instability modes, triggered by modulating the rotor rotation speed. Quaranta et al. [22] extended their previous work to a system of two interlaced helices shed from a two-bladed rotor. In addition to local pairing triggered by rotor speed modulation, global pairing was induced by introducing a slight eccentricity to the rotor.

In the present investigation, a detailed numerical study of the wake generated by multiple configurations of a two-bladed model rotor with different degrees of asymmetry between the blades will be presented. The focus is on investigating the tip vortex formation, its parameterization and its stability, using the DTU multi-fidelity vortex code **MIRAS** [23, 24, 25, 26]. The investigation includes a detailed validation of the solver against water channel measurements performed by Quaranta el al. [22] and a new high-resolution measurement campaign carried out by the authors at the IRPHE-CNRS facilities and first presented in what follows. As mentioned above, the work aims at setting the groundwork for future instability studies with **MIRAS**. Vortex methods can be considered to have a level of fidelity between fully-resolved computational fluid dynamics (CFD) and blade element momentum (BEM) methods, although in reality this can vary substantially depending on the aerodynamic and flow models employed in the simulation. With vortex solvers, it is possible to easily combine different blade aerodynamic models, depending on the degree of accuracy required for the case of study. Enumerated in ascending complexity, the aerodynamic models traditionally implemented in vortex solvers can be classified as: lifting-line (**LL**), lifting-surface, potential-panel, viscous-inviscid-panel and penalization methods. Analogously, one could divide the flow solvers into the following categories: prescribed filament wake methods, free wake filament methods, hybrid filament-particle-mesh methods, and particle-mesh methods.

In the current work, the blade aerodynamics are simulated with a **LL** model in combination with two different flow models based on the vortex-in-cell approach [27, 28, 29, 30]. In this study, the two flow models are compared, emphasizing the level of accuracy required to capture the different physical phenomena observed in the experimental campaign. The first model is an inviscid one where the filament structure of a free-wake method is maintained and combined with a particle-mesh for speeding up the simulations [25] (referred to hereafter as the hybrid-filament method). The higher-fidelity model accounts for viscous stretching and diffusion by using a finite-difference approach to resolve the vorticity transport equation [26], which is obtained by taking the curl of the Navier-Stokes equations, and describes the evolution of the vorticity of a fluid particle as it moves with the flow. This method is referred to as the particle-mesh method hereafter.

The investigation focuses on assessing the ability of the models to predict the different flow features observed in the rotor wake during the experimental campaign. A number of base states are taken into account, including four different tip speed ratios. First, the focus lies on the tip vortex characterization in the near wake region, i.e. vortex strength and location. The models' ability to capture the general flow characteristics is estimated by means of comparing simulated vorticity and velocity distributions with results from experimental Particle Image Velocimetry (PIV) measurements. An important research question here is if it is possible to accurately capture the tip vortex roll-up process, including the viscous core profile formation and its variation in time. Finally, the models' ability to predict the leapfrogging location between consecutive tip vortices is evaluated for different levels of rotor asymmetry and under different flow conditions.

The manuscript is organized as follows. Section 2 describes the numerical methods employed in the investigation, including the **LL** model and the different flow solvers. The experimental configuration is described in Section 3, and Section 4 introduces the numerical setup, including the wind turbine

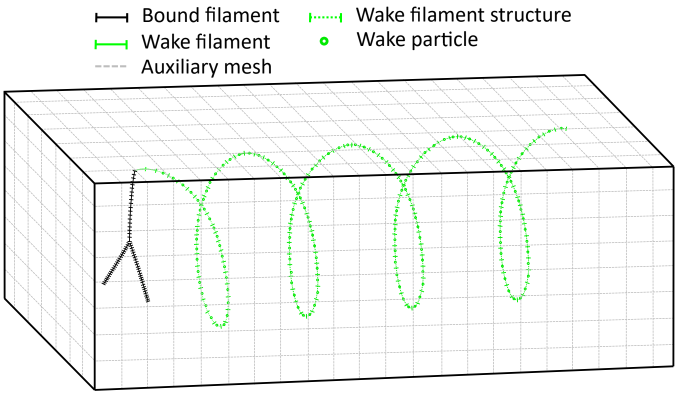

Figure 1: Sketch relating to the lower-fidelity hybrid-filament method. For simplicity only the tip filament shed by one of the blades is included.

model, the discretization and the domain size of the simulation. Results for the unperturbed rotor configuration at different tip speed ratios and with different model fidelities are presented in Section 5.1. Finally, the effect of introducing a perturbation in the vortex system in the form of a radial offset of the two-bladed rotor are shown in Section 5.2. The conclusions are summarized in Section 6.

2. Numerical methods

The DTU in-house vortex code **MIRAS** [23, 24, 25, 26], i.e., Method for Interactive Rotor Aerodynamic Simulations, is a multi-fidelity aerodynamic tool for wind turbine performance analysis. The flow solver can be divided into two parts: an aerodynamic model and a wake/flow model. In the present study, the lifting line module is used as the aerodynamic model, in which airfoil data and the actual geometry are the primary inputs used to determine the loading on the rotor blades. The wake generated by the turbine is modelled following two different implementations with varying levels of complexity.

Lower-fidelity simulations are performed following a similar approach to the one presented in [25]. In this case, the inviscid panel method is substituted by a lifting line model to represent the blades. The method can be seen as an enhanced free-wake model, were the vortex filament structure emanating along the span of the lifting line is maintained throughout the domain and an auxiliary Cartesian mesh is used to speed up the induction calculations

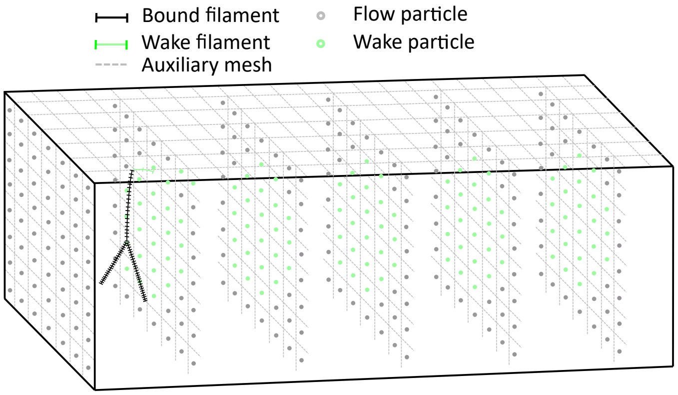

Figure 2: Sketch relating to the higher-fidelity particle-mesh method. For simplicity only selected mesh sections are depicted.

between vortex elements via a Fast Fourier Transform (FFT) based method developed by Hejlesen et al. [31, 30]. In the following, this approach, sketched in Figure 1, is referred to as a hybrid-filament method or HFM. In general, this implementation works on a coarser mesh and with a lower particle count.

Higher-fidelity simulations are performed using the same implementation as the one presented in [26, 32]. This implementation is referred to as particle-mesh method or PMM hereafter. In the particle-mesh method, the vorticity transport equation, which can be seen as the vorticity formulated Navier–Stokes equation, is resolved using finite differences in the underlying mesh. It is able to accurately account for vortex stretching and viscous diffusion through a particle re-meshing scheme. Such scheme generates a much larger particle count if compared to the lower-fidelity model, although it is necessary to ensure a smooth vorticity field throughout the auxiliary mesh. Note that, as part of the investigation, simulations were performed using a single-coefficient Smagorinsky sub-grid scale model (SGS) [33], with two different implementations, as in [34]: one acting on the full vorticity field, and the other one acting on the small-scale vorticity field. No notable differences were observed compared to simulations without the SGS model in the region of interest of the present investigation, i.e. the near- and mid-wake region. A sketch of the particle-mesh method is depicted in Figure 2.

The blade aerodynamic model (**LL**) relies in this case on two-dimensional polar data for lift, drag and pitching moment of the blade profile (see Figure 5 below). The rotor blades are modelled by a line of discrete vortex filaments to account for the bound vortex strength and to release vorticity into the flow. Such vorticity is released due to spanwise and temporal variations of the bound vortex, and it is commonly known as trailing and shed vorticity, respectively. The Kutta–Joukowsky theorem is used to calculate the strength γ (circulation) of the bound vortex along the blade span:

$$\gamma = \frac{L}{\rho V_{qc}} \tag{1}$$

where L is the lift force (per unit span) of each aerodynamic section, and is obtained by interpolation from a set of tabulated airfoil data (lift, drag and moment coefficients; C_l, C_d and C_m) as function of the computed angle of attack. The air density at a given temperature is represented by ρ. The total velocity magnitude computed at the quarter chord of the different blade sections is V_{qc}. It results from the combination of the inflow velocity, the blade motion, the velocity induced by the wake and a bound vortex correction in the case of curved blade geometries.

Newton's method is used to attain the desired convergence in the blade forcing, which is found once the residual of V_{qc} in all lifting line control points is lower than 10^{-3}. A constant under-relaxation factor of 0.10 is used to update the velocity components, and convergence is usually attained within a few iterations. The first set of vortex elements is released in the chord direction at each spanwise station.

The initial sheet of vortex filaments is transformed into a set of vortex particles whose vorticity is later interpolated onto an auxiliary Cartesian mesh. The downstream location of the filament-to-particle transformation depends on the problem specifications and the choice of flow solver, and is defined by the user. Note again that in the hybrid-filament approach the filament structure is maintained throughout the domain, whereas in the particle-mesh approach it is not. The motion of the vortex elements is determined by the velocity of their markers $\underline{u}(\underline{x}_i)$ (the filament end points or the particle itself). Such a velocity is calculated by superposition of the free-stream velocity $\underline{U}_0$ and the velocity contributions from all free and bound vortex elements at the marker positions $\underline{x}_i$:

$$\frac{d\underline{x}_i}{dt} = \underline{u}(\underline{x}_i) \qquad \text{with} \qquad \underline{u}(\underline{x}_i) = \underline{U}_0 + \underline{u}_\Gamma(\underline{x}_i) + \underline{u}_{\mathrm{fw}}(\underline{x}_i) + \underline{u}_{\mathrm{pw}}(\underline{x}_i) \tag{2}$$

where $\underline{u}_\Gamma$ is the velocity induced by the blade bound vortex, $\underline{u}_{\mathrm{fw}}$ is the velocity induced by the filament-based wake and $\underline{u}_{\mathrm{pw}}$ is the velocity induced by the particle-based wake. The calculation of the different velocity contributions of Equation (2), as well as a study on the choice of the time-integration scheme, was detailed in previous work by the authors [25, 26]. During the present study, it has been found that a higher-order time scheme was necessary in the particle-mesh simulations (second-order Runge-Kutta or higher), in order to correctly capture the roll-up process of the tip vortices. Moreover, it was found that the roll-up plays an important role in the correct prediction of the vortex core size and its growth rate. Both quantities are considerably over-predicted when using a first-order Euler scheme.

In both fidelities, the vortex elements' strengths are interpolated onto a Cartesian mesh, where their interaction is efficiently calculated by an FFT-based method. Whereas this is the only use of the auxiliary mesh in the hybrid-filament model, the vorticity transport equation is resolved in the mesh using finite differences in the particle-mesh solver. The vorticity transport equation describes the evolution of the vorticity of a fluid particle as it moves with the flow. It is obtained by taking the curl of the Navier-Stokes equation and, assuming an incompressible fluid with a constant and uniform viscosity, it reads

$$\frac{D\underline{\omega}}{Dt} = \frac{\partial \underline{\omega}}{\partial t} + \left(\underline{u} \cdot \nabla\right) \underline{\omega} = \left(\underline{\omega} \cdot \nabla\right) \underline{u} + \nu \nabla^2 \underline{\omega} \tag{3}$$

The rate of change of the vorticity, $\frac{\partial \underline{\omega}}{\partial t}$, together with the convection term, $\left(\underline{u} \cdot \nabla\right) \underline{\omega}$, which accounts for the changes in vorticity due to the motion of the fluid particle, appear on the left hand side. On the right hand side, $\left(\underline{\omega} \cdot \nabla\right) \underline{u}$, accounts for the vortex stretching and tilting, while $\nu \nabla^2 \underline{\omega}$ represents the vorticity diffusion due to viscous effects.

Finally, it is important to note that blockage effects arising from the vicinity of the domain boundaries are avoided by solving the Poisson equation using a regularized Green's function solution with free-space boundary conditions in all directions. A tenth-order Gaussian filter is used to regularize the singular free-space Green's function, obtaining a higher-order approximation. A filter function of width 1.5Δ, where Δ is the mesh cell size, is chosen to minimize the smoothing error associated with the regularization, while resolving the filter function accurately.

3. Experimental setup

The experiments used to validate the numerical simulations were conducted in a recirculating free-surface water channel. The set-up is described

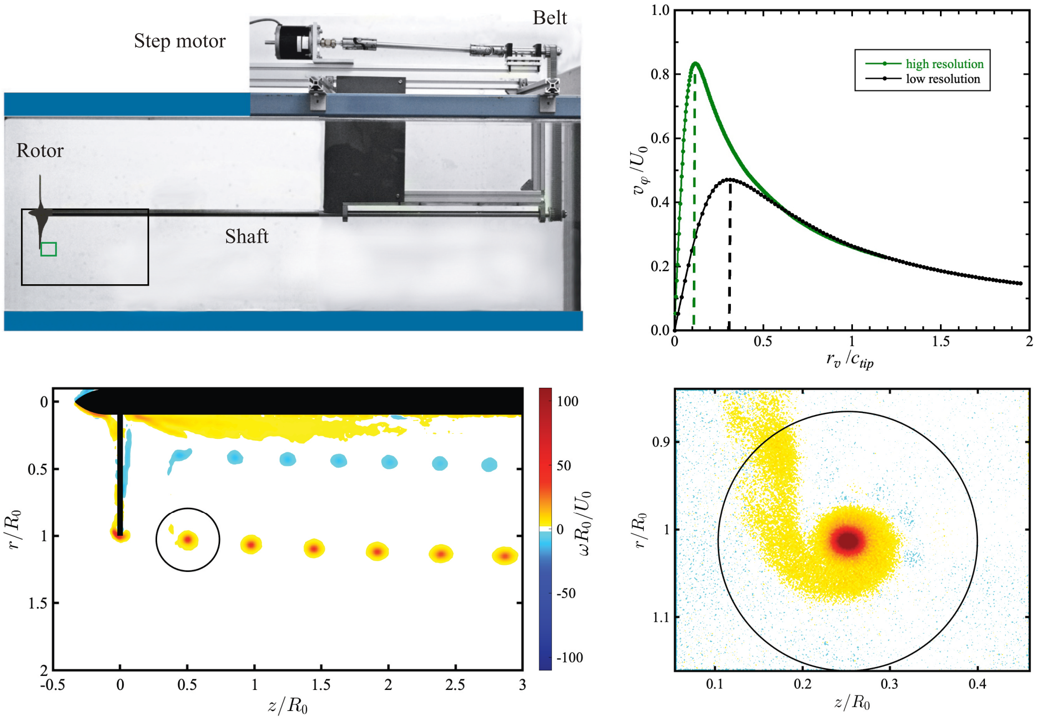

Figure 3: Top left: Experiment setup, including the large and small fields of view used for PIV measurements indicated in black and green, respectively. Bottom left: Vorticity field from the large field of view (low resolution), with a circle whose diameter is given by the vortex spacing h, indicating the region used to analyze the blade tip vortex properties. Bottom right: Vorticity field from the small field of view (high resolution) showing a single vortex in high resolution. Top right: Comparison between the swirl velocity profiles of the blade tip vortex calculated using the two resolutions. The dashed lines indicated the core radius.

in detail by Quaranta et al. [22], but a summary is provided here. The water channel test section size is 150 cm × 38 cm × 50 cm (length × width × height). A two-bladed rotor was mounted on a 15 mm-diameter shaft extending 95 cm downstream, where it was connected to a computer-controlled stepper motor through a gearbox (Figure 3). The rotor had a radius of R_0 = 80 mm and a tip chord of c_{tip} = 10 mm, and was designed to approximate a Joukowsky rotor over the outer 75% of the radius. The low-Reynolds number A18 airfoil [35] formed the cross-sections along the entire blade.

The helical vortex system shed from the rotor blade tips could be perturbed by slightly offsetting, by an amount δ, the alignment of the rotor with

λ	U_0 [cm/s]	f [Hz]	δ [cm]	Re
4.47	45.0	4.0	0.122	2.0×10^4
5.49	36.6	4.0	0.122	2.0×10^4
6.70	30.0	4.0	0.122	2.0×10^4
8.04	25.0	4.0	0.122	2.0×10^4
5.52	45.5	5.0	**0.02**	2.5×10^4
5.52	45.5	5.0	**0.07**	2.5×10^4
5.52	45.5	5.0	**0.13**	2.5×10^4
5.52	45.5	5.0	**0.21**	2.5×10^4

Table 1: Summary of the parameters for the experiments conducted on the model two-bladed rotor. The tip speed ratio λ was varied in the first set of measurements, and the the radial offset δ in the second set.

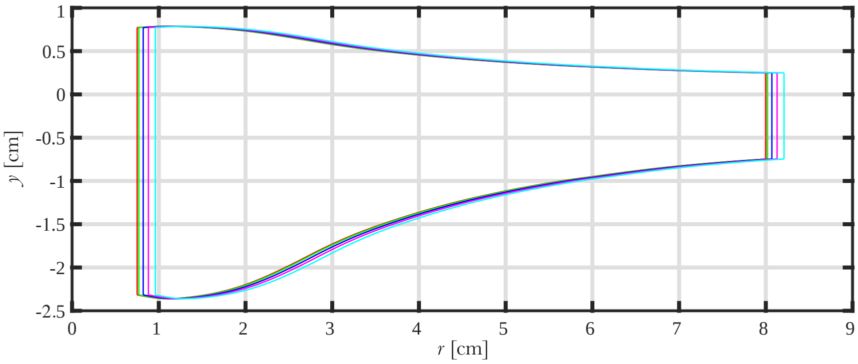

Figure 4: Sketch of the baseline blade planform and the different offset alignments. Baseline [—], δ = 0.2 mm [—], δ = 0.7 mm [—], δ = 1.3 mm [—] and δ = 2.1 mm [—].

the shaft. The resulting difference in radial positions of the two blades, 2δ, was of the order of a few millimeters. A range of values of δ for different tip speed ratios λ (= $2\pi R_0 f/U_0$, with f being the rotor frequency and U_0 the free-stream velocity), were tested, as summarized in Table 1 and sketched in Figure 4. Table 1 also includes the values of tip chord-based Reynolds number ($Re = 2\pi f R_0 c_{tip}/\nu$) for each case. To visualize the vortices, the rotor blade tips were painted with fluorescent dye, which was then illuminated by the light from an argon-ion laser. Quantitative measurements of the velocity and vorticity fields in the center-plane of the wake were obtained using PIV. These measurements had a vector resolution of 1.35 mm and spanned approximately $-0.5 < z/R_0 < 3$ and $0 < r/R_0 < 2$ (see Figure 3 bottom left), where z and r are the downstream and radial coordinates measured from the rotor center.

An additional high-resolution PIV measurement was conducted on the symmetric rotor to capture the vortex core more accurately (Figure 3 bottom right). The experimental procedure was similar to that of the lower resolution experiments, though the camera was brought closer to the test section to reduce the field of view to $0.42R_0 \times 0.33R_0$. The particle images were processed using an in-house code developed by Meunier and Leweke [36], as described by Quaranta et al. [20]. The correlation was performed in an iterative process, with the first calculation using 64 × 64 pixel windows with 50% overlap. Window displacement and deformation based on the preliminary vector field was performed before the second calculation, which used 16 × 16 pixel windows with 50% overlap, resulting in a vector resolution of 0.08 mm. The rotor was run at a tip speed ratio of $\lambda = 5.49$, and the field of view was centered on the most recently shed tip vortex at a wake age of 90°. This high-resolution measurement yielded a core radius (see section 5.1.2 below), of $a_{\max} = 1.1$ mm. This is significantly smaller than the value $a_{\max} = 3.1$ mm reported by Quaranta et al. [22] based on the lower-resolution measurements, which were unable to fully resolve the vortex core.

4. Numerical setup

This section describes the computational setup used for both the aerodynamic model and the two flow models employed.

4.1. General parameters

All simulations have been performed on a $15R_0 \times 4R_0 \times 4R_0$ Cartesian mesh with free boundary conditions in all directions. In the **LL** model, the blade is represented by a bound vortex discretized with 80 straight segments of equal length. The lift and drag coefficients used are depicted in Figure 5 as function of the angle of attack. These coefficients may not perfectly represent the true coefficients of the experimental airfoil, due to the following reasons: possible modification of the original airfoil geometry during the manufacturing process; differences in the turbulence intensity level of the water channel compared to the one in the wind tunnel where the coefficients were obtained; varying Reynolds number along the span in the experiment, not accounted for in the simulations; slightly lower Reynolds number in the water channel.

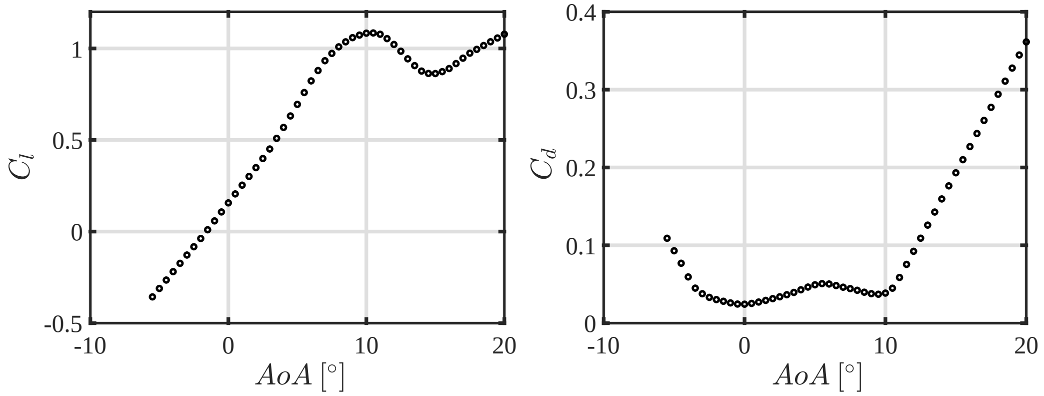

Figure 5: Lift (left) and drag (right) coefficient of the A18 airfoil as function of the angle of attack (AoA). The drag coefficients are obtained using XFOIL [37] while the lift values are measurements by Selig et al. [35] at a Reynolds number of 30000.

A final source of disagreement between the numerical model and the experiments is the hub and shaft geometry, which has not been modeled, leaving an empty space between the blades ($r < 1$ cm) and generating a higher-velocity region in the center of the rotor. Although the shaft boundary layer has a stabilizing effect on the root vortex, this effect is only appreciated outside the region of interest of the present investigation. The impact of the hub and shaft geometry on the tip vortex properties is assumed to be minimal.

The blockage effect due to the lateral confinement of the flow by the water channel walls is not modelled in the numerical setup. The flow velocity measured along the streamwise direction at a radial location of $r/R_0 = 2$ is shown in Figure 6. In the figure, it can be observed that the velocity increases with the downstream position due to the wall effect. In an effort to partly account for this effect in the simulations, the velocity measured at $z/R_0 = 0$ was used as the free-stream velocity (U_0) in all numerical cases. In general this velocity was about 2.8 % larger than the free-stream velocity reported in the experimental campaign of Quaranta el al. [22]. This modification allowed the unbounded solver to model the correct flow conditions around the blade, and therefore reproduce the correct vortex properties. As seen in the figure, the outer velocity continues to evolve (increase) further downstream, which will affect the convection velocity of the vortex system and therefore its spatial evolution.

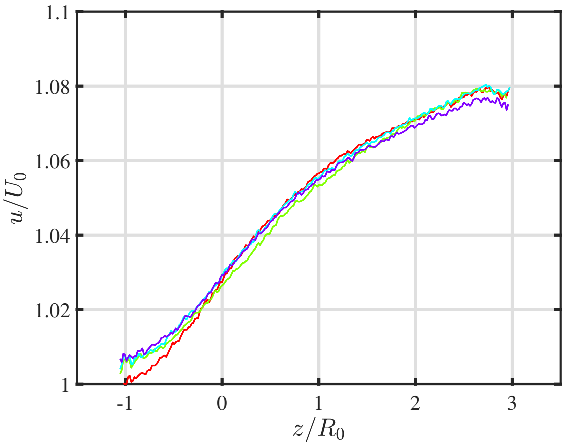

Figure 6: Evolution of the free-stream velocity measured at $r/R_0 = 2$, for $\lambda = 4.47$ [—], $\lambda = 5.49$ [—], $\lambda = 6.70$ [—] and $\lambda = 8.04$ [—]

4.2. High-resolution particle-mesh parameters

For the particle-mesh case, a constant cell size of 0.1 cm has been used in the $x-$, $y-$ and $z-$directions, which adds up to a total of more than 118 million cells. The simulations have been performed with an azimuthal discretization of 1° and a total of 8000 time steps. During the present investigation, it has been found that a finer resolution is necessary to correctly capture the vortex core structure, both numerically and experimentally. A finer mesh with a cell size of 0.05 cm and the same outer boundaries is therefore used for a single unperturbed case at the tip speed ratio of 5.49. In this case, the total number of cells increases to more than 950 million, with a similar number of vortex particles. The azimuthal discretization has been reduced to 0.5°, in order to maintain the same Courant–Friedrichs–Lewy number (CFL). Note that a CFL value lower than 2 is assumed reasonable since vortex methods have less strict CFL conditions than Eulerian solvers [38, 39, 40]. Table 2 shows an overview of the parameters for the simulations performed in the investigation with the non-perturbed rotor. An eighth-order stencil is used to spatially discretize the vorticity equation. Moreover, a particle re-meshing is forced every time step to maintain a smooth field, and a periodic regularization and re-projection of the vorticity field is applied with the same frequency to keep the field divergence-free. A tenth-order Gaussian regularization kernel is used for the smoothing of the vorticity field. A third-order Runge-Kutta time stepping method has been used.

Method	λ	$\Delta\theta$ [°]	Δt [ms]	N_t	Δ [cm]	CFL	$N_c \times 10^{-6}$
HFM	4.47	2	1.38	4000	0.4	0.6937	1.8
HFM	5.49	2	1.38	4000	0.4	0.6937	1.8
HFM	6.70	2	1.38	4000	0.4	0.6937	1.8
HFM	8.04	2	1.38	4000	0.4	0.6937	1.8
PMM	4.47	1	0.694	8000	0.1	1.3954	118
PMM	5.49	1	0.694	8000	0.1	1.3954	118
PMM	6.70	1	0.694	8000	0.1	1.3954	118
PMM	8.04	1	0.694	8000	0.1	1.3954	118
PMM	5.49	0.5	0.347	16000	0.05	1.3954	950

Table 2: Overview of the parameters used for the simulations with the non-perturbed rotor configuration. $\Delta\theta$ denotes the azimuthal discretization, Δt the time step size, N_t the total number of simulated time steps, Δ is the cell size, CFL the Courant–Friedrichs–Lewy number and N_c the total number of cells/vortices.

4.3. Low-resolution hybrid-filament wake parameters

In the hybrid-filament model, a constant spacing of 0.4 cm in all directions was used in all cases, adding up to a total of 1.856 million cells. The simulations have been performed with an azimuthal discretization of 2° and a total of 4000 time steps. A first-order Euler scheme was used in the time updating procedure. No vortex core or core growth models were used in this case, contrary to what is normally done in free-wake models. The auxiliary mesh takes care of the filament interaction and helps to avoid singularities between too closely located vortex elements. We have used the knowledge obtained from our previous studies with the hybrid-filament method to setup the model specifications. For example, a very detailed discretization study for the hybrid-filament method was carried out by the authors in [25]. In that paper we analyzed the influence of both the time step and the cell size, among other model features in both the aerodynamic loading and the flow on a model rotor. Results from MIRAS simulations were successfully validated against wind tunnel PIV measurements [41].

5. Results and discussion

First, a comparison between simulation and experiment is performed for the unperturbed case at different tip speed ratios. Both levels of fidelity are used to predict the general tip vortex characteristics, such as their location and strength. Second, a direct flow comparison of the solver predictions against PIV measurements for the instantaneous and mean velocity and vorticity fields is carried out for the case with a 1 mm resolution, followed by a comparison of the detailed vortex profile. This comparison is primarily conducted using the particle-mesh approach, since such a fidelity level is required to accurately capture the detailed flow features observed in the rotor wake. Note that contrary to standard free-wake codes, such as in Scully et al. [42], where a viscous core model is used in combination with a core growth model, the particle-mesh approach is capable of simulating the viscous core formation and its growth in time without the need for a specific sub-model. A detailed comparison of the core profile is made between the higher-resolution experiments and simulations. Finally, two studies involving asymmetric rotors are presented, the first investigating the effect of tip speed ratio and the second focusing on the influence of the perturbation magnitude. Here the emphasis is on capability of the solvers to predict the evolution of the perturbation observed in the experimental campaign.

5.1. Unperturbed rotor case

Four tip speed ratios are considered: $\lambda = 4.47$, 5.49, 6.70 and 8.04. The comparison is divided in subsections: tip vortex characterization, instantaneous vorticity fields, and mean velocity and vorticity fields.

5.1.1. Tip vortex characterization

The helical tip vortex system in the wake of a rotor is characterised by a number of parameters: the streamwise vortex separation (h), which depends on the helix pitch and the number of vortices; the vortex core size (a_{max}), which is the distance between the vortex center and the location of maximum swirl velocity; the vortex strength or circulation (Γ); and the radial expansion (r/R_0) as function of downstream distance. The computed tip vortex locations in the radial and streamwise directions (r/R_0 and z/R_0, respectively), using a quadratic fit around the location of maximum vorticity for subgrid accuracy, is depicted in Figure 7. In comparison with the experimentally obtained values, both numerical models predict a lower expansion of the wake, with the hybrid-filament model predicting very small differences between the various tip speed ratios, and the particle-mesh model predicting virtually no expansion for the $\lambda = 4.47$ case. A possible explanation for the discrepancies between the simulations and experiments can be the higher mass flow in the

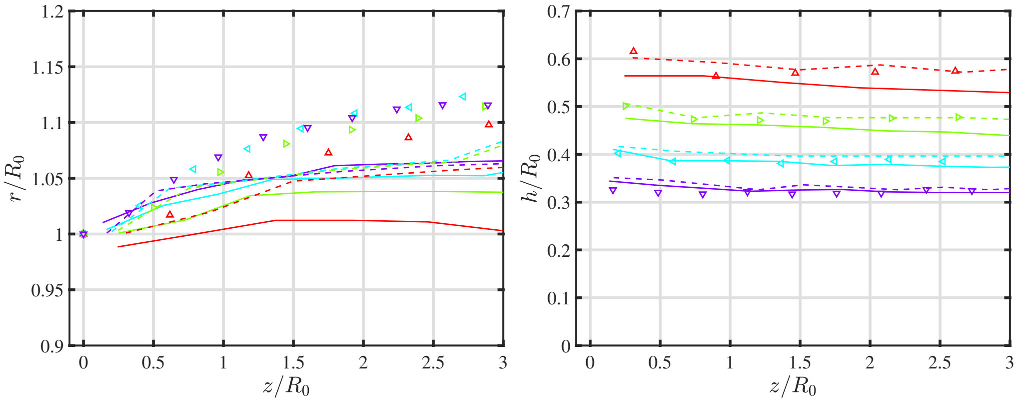

Figure 7: Evolution of the tip vortex characteristics, comparing simulations to experiments. Left: non-dimensional radial location. Right: non-dimensional streamwise vortex separation.
Experiments: $\lambda = 4.47$ [△], $\lambda = 5.49$ [▷], $\lambda = 6.70$ [◁], $\lambda = 8.04$ [▽].
Particle-mesh simulations: $\lambda = 4.47$ [—], $\lambda = 5.49$ [—], $\lambda = 6.70$ [—], $\lambda = 8.04$ [—].
Hybrid-filament simulations: $\lambda = 4.47$ [--], $\lambda = 5.49$ [--], $\lambda = 6.70$ [--], $\lambda = 8.04$ [--].

wake due to the absence of the shaft in the simulations. A better agreement is obtained between measurements and simulations regarding the distance h between tip vortices. It is observed that differences between the solvers in the prediction of the vortex location increase with the decreasing tip speed ratio, although the maximum difference never exceeds the 6% mark.

Figure 8 depicts the vortex circulation obtained from the experimental data compared to the two numerical models. The circulation is computed by integrating the velocity field on a circular path of radius equal to half the vortex separation distance, $h/2$, at each one of the tip vortex center locations. In all cases the numerical simulations under-predict the vortex circulation, which can be a direct consequence of the polar data used. It has been confirmed by the authors, using the XFOIL software [37], that the use of tripped boundary layer considerably increases the lift coefficient in the linear region. Such a sensitivity of the airfoil under turbulent conditions can explain the observed differences in the circulation. Very similar circulation values are predicted by both solvers at $\lambda = 5.49$ and higher, but the particle-mesh model better captures the vortex strength at $\lambda = 4.47$. It is expected that the roll-up process is much better captured by the particle based method since it models vortex stretching much more accurately by resolving the vorticity transport

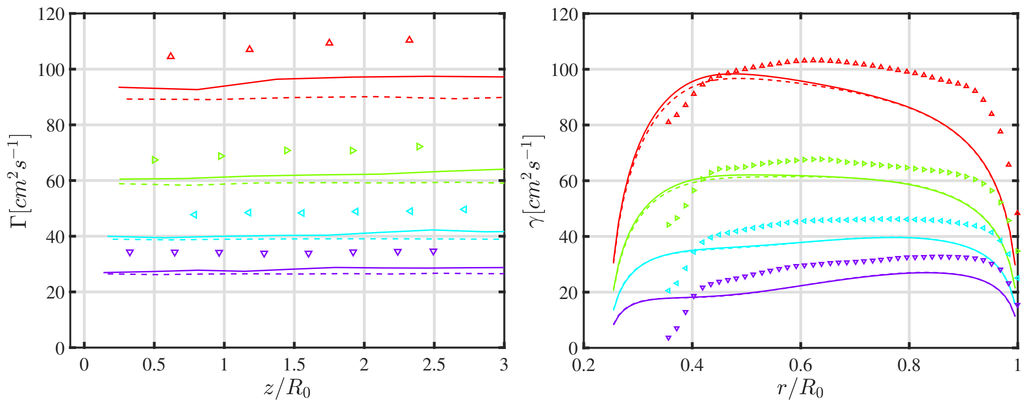

Figure 8: Left: evolution of the tip vortex circulation. Right: spanwise distribution of the blade bound circulation.
Experiments: $\lambda = 4.47$ [△], $\lambda = 5.49$ [▷], $\lambda = 6.70$ [◁], $\lambda = 8.04$ [▽].
Particle-mesh simulations: $\lambda = 4.47$ [–], $\lambda = 5.49$ [–], $\lambda = 6.70$ [–], $\lambda = 8.04$ [–].
Hybrid-filament simulations: $\lambda = 4.47$ [--], $\lambda = 5.49$ [--], $\lambda = 6.70$ [--], $\lambda = 8.04$ [--].

equation.

The radial distribution of the blade circulation, as computed by the particle-mesh and hybrid-filament solvers, is also depicted in Figure 8. Focusing on the $\lambda = 4.47$ case, we can see how the difference in the tip vortex circulation does not appear as clearly in the blade circulation distribution. Not surprisingly, the value of the circulation of the vortices in the wake is almost identical to the maximum value of the blade bound circulation. From the experimental data, the circulation distribution is obtained by integrating the vorticity in a radial strip located at a distance h behind the rotor plane, in order to ensure that the vorticity layer is fully established. The radial coordinate was corrected for wake expansion, starting at $r/R_0 = 1.5$ and going inwards. In the root region, the decrease in the circulation is observed further outwards in the experiments due to the influence of the shaft boundary layer. Moreover, this boundary layer leads to an increase in the experimental circulation below $r/R_0 = 0.3$, which is not shown in the comparison. In the mid- and outer region of the blade, the difference between experiments and simulations appears to be a constant radial offset. This could indicate an offset in the linear region of the lift curve used in the numerical models, compared to the experimental one attained in the water channel.

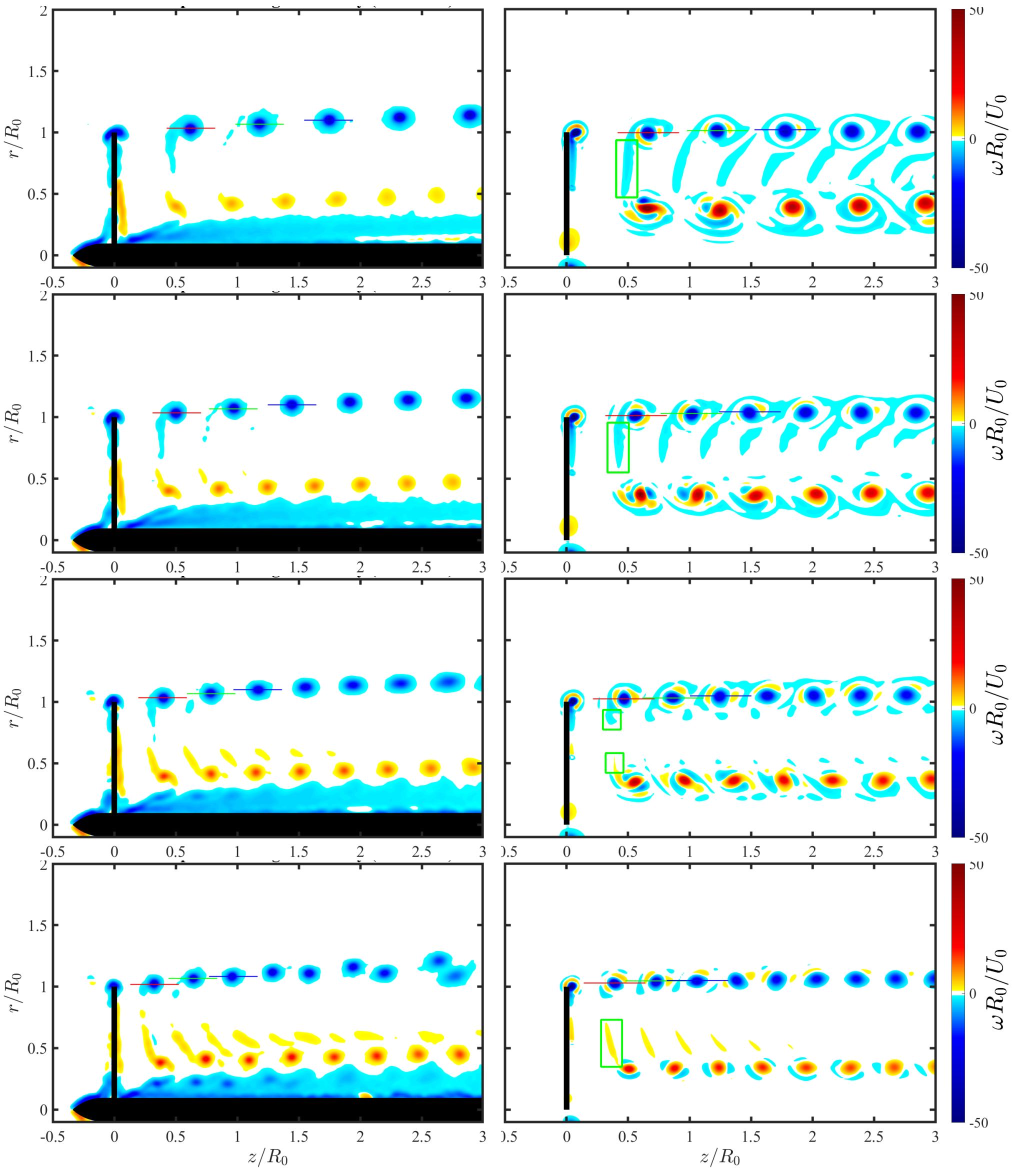

Figure 9: Instantaneous non-dimensional out-of-plane vorticity, $\omega_y R_0/U_0$ for tip speed rations (from top to bottom) λ = 4.47, 5.49, 6.70 and 8.04. Left: PIV measurements; right: numerical simulations using the particle-mesh method.

5.1.2. Instantaneous vorticity field

The particle-mesh model is used in a more detailed comparison of the flow characteristics with experimental PIV data. For the experimental data, the phase-locked average of 300 instantaneous PIV vorticity fields is used to average out the random fluctuations caused by the very low (<1%) level of turbulence in the water channel. In the particle-mesh simulations, zero inflow turbulence intensity is prescribed, so the flow is fully determined by the periodic motion of the rotor and the instantaneous vorticity field is equal to the phase-averaged one. The wake topology change with varying tip speed ratio can be appreciated from the vorticity fields shown in Figure 9. The comparison shows an overall good agreement between the experimental and numerical results, with the main difference appearing in the strength of the root vortex, which is clearly over-predicted by the solver. This over-prediction is mainly due to the vorticity-cancellation effect of the shaft boundary layer, which is not included in the numerical simulations, as can also be observed in the figure. Note that the location of both root and tip vortices is generally well captured by the particle-mesh solver. Moreover, a vortex sheet attached to the tip and root vortices is seen in the PIV measurements and is also captured in the numerical model , as highlighted by the green rectangles in the plot. At low tip speed ratios, this sheet has the same sign as the tip vortex, while as the tip speed ratio increases, the sheet shifts toward the root and changes its sign. The behavior of this sheet is related to the blade circulation distribution shown earlier in Figure 8.

The tip vortex velocity and vorticity profiles at $\lambda = 5.49$ are shown in Figure 10 for the first three tip vortices marked in Figure 9 with colored horizontal lines. Note that such lines are used to extract the depicted values of vorticity and velocity across the vortex core. In this case, an equivalent resolution is used in both PIV and simulations. Although it is known that this resolution is too coarse to accurately capture the vortex core profile, it is the only way to measure multiple vortices in the same PIV window due to resolution constraints. A fairly good agreement is obtained between experiments and simulations, although the reduction in the maximum core vorticity with the downstream position of the vortex predicted by the solver is not observed in the PIV data. Regarding the velocity profile, a similarly good agreement is obtained, with the solver capturing the increased velocity in the outer bounds of the first tip vortex (in red), which can be related to the still ongoing roll-up process. Moreover, judging from the velocity distribution, the core size predicted by the simulations has a very similar magnitude as the experimental one for this level of resolution.

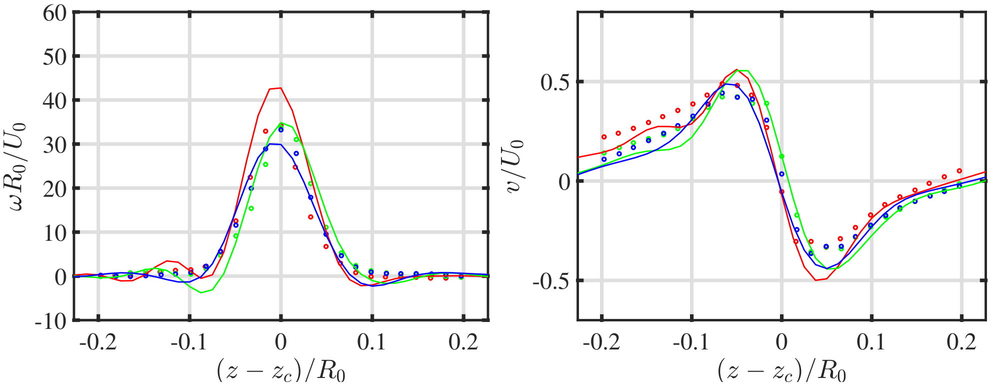

Figure 10: Comparison between PIV measurements and numerical simulations of the first three tip vortex (TV) core profiles for $\lambda = 5.49$. Left: vorticity profile, $\omega R_0/U_0$; right: velocity profile, v/U_0. z_c is the downstream position of the respective vortex center. PIV measurements (0.9 mm resolution): 1st TV [○], 2nd TV [○], 3rd TV [○]. Numerical simulations (1.0 mm cell size): 1st TV [–], 2nd TV [–], 3rd TV [–].

A finer resolution is needed in both the PIV measurements and the numerical method to more accurately capture the core profile of the tip vortex. Unfortunately, in order to accommodate such resolution in the PIV measurements, a smaller window is necessary. This means that only one vortex at a time can be investigated with a pixel resolution of 0.001 cm (PIV vector resolution 0.008 cm). On the other hand, in simulations one can not reduce the domain size without compromising the accuracy of the method (i.e., a domain shortening in the streamwise direction would reduce the induction at the rotor plane and therefore increase the blade loading/circulation). A finer resolution is also used in the simulations, but due to computational restrictions it is not possible to refine to the same cell size as in measurements. A cell size of 0.05 cm is used, the same outer domain is maintained, and the time step is reduced by half in order to keep the CFL number unchanged. This adds up to more than 950 million cells and such simulation uses a plethora of computational resources (800 cores during more than 69 hours). The study is therefore limited to the one tip speed ratio $\lambda = 5.49$, with the simulated evolution of the first eight tip vortices presented in Figure 11.

Figure 12 shows the swirl velocity profiles of the vortices in Figure 11, representing a wake age range between 65° and 1325°. They were obtained by interpolating the simulated velocity field onto polar grids centred on each vortex and averaging the projected azimuthal velocity component in the az-

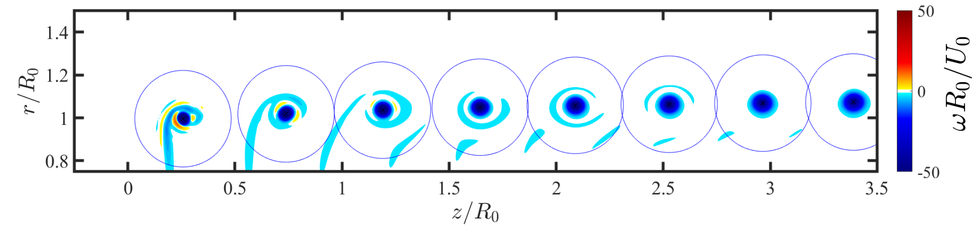

Figure 11: Instantaneous vorticity field in the tip vortex region, as predicted by the particle-mesh simulations, for the case with $\lambda = 5.49$ and a cell size of 0.05 cm. Blue circles depict the perimeters of the polar grids centered on each vortex and used in the swirl velocity calculation.

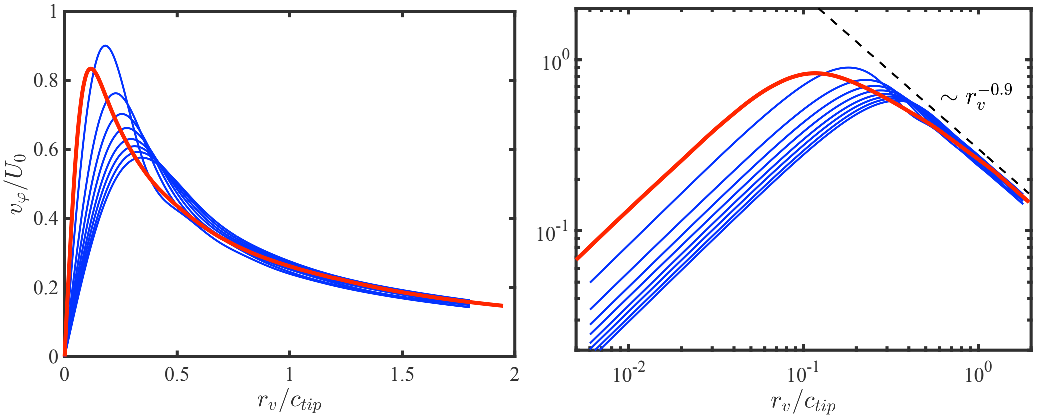

Figure 12: Vortex core velocity profiles for $\lambda = 5.49$. Comparison between high-resolution particle-mesh simulations (Δ = 0.05 cm) [—] and high-resolution PIV measurements (vector resolution of 0.008 cm) [—]. Left: linear scale, right: log-log scale.

imuthal direction of this grid for each radius. Figure 12 also contains the experimental result from the high-resolution PIV measurements shown in Figure 3, obtained for a tip vortex at wake age 90°. Good agreement between experiment and simulation is found in the outer part of the profiles, where the swirl velocity varies approximately as $r_v^{-0.9}$. The maximum swirl velocity is also of the same order in the early stage of the wake evolution, around 80% of the free-stream velocity. However, the profiles differ significantly in the core region near the vortex axis.

One well-defined measure of the vortex core size is the radius of maximum

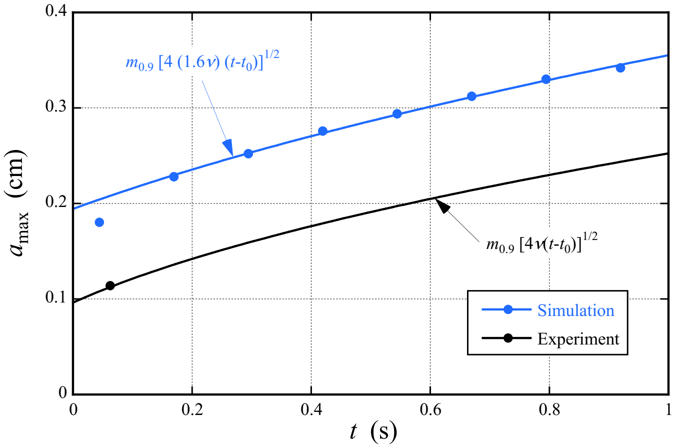

Figure 13: Vortex core size evolution for $\lambda = 5.49$, as obtained from the high-resolution particle-mesh simulations [•] and experimental PIV measurements [•]. Solid lines in black and blue represent the theoretical vortex core growth given by the equations reported in the figure ($m_{0.9} = 1.167$).

swirl velocity, $a_{\max}$. It is easily detectable in numerical or experimental velocity profiles, such as those in Figure 12. From the theoretical viscous evolution of an axisymmetric velocity profile initially (at time $t = t_0$) proportional to r_v^{-n}, found e.g. in [43, 44], one can obtain the following relation:

$$a_{\max} = m_n \left[4\nu(t - t_0)\right]^{1/2}, \tag{4}$$

where m_n is a constant that depends on the exponent n of the outer velocity profile. According to (4), the core radius increases with the square-root of time due to the viscous diffusion of vorticity. When the core radius obtained in our simulations is plotted as function of time, as depicted in Figure 13, the square-root variation is roughly found, but with a growth rate that corresponds to a viscosity which is slightly higher than the actual fluid viscosity (1.6ν). Note that the first vortex has been left out of the simulation fit, since, as depicted in Figure 11, the roll-up process is still underway. Overall, simulations with $\Delta = 0.05$ cm show a larger core size than the PIV measurements with a 0.008 cm resolution, although the core growth rate is very similar. This discrepancy in core size highlights the necessity of a mesh with an even higher resolution (and a corresponding smaller time step to maintain the CFL condition), which is beyond our current computational limits. Using a resolution of 0.01 cm in the present numerical setup would require a mesh with more than 118 billion cells.

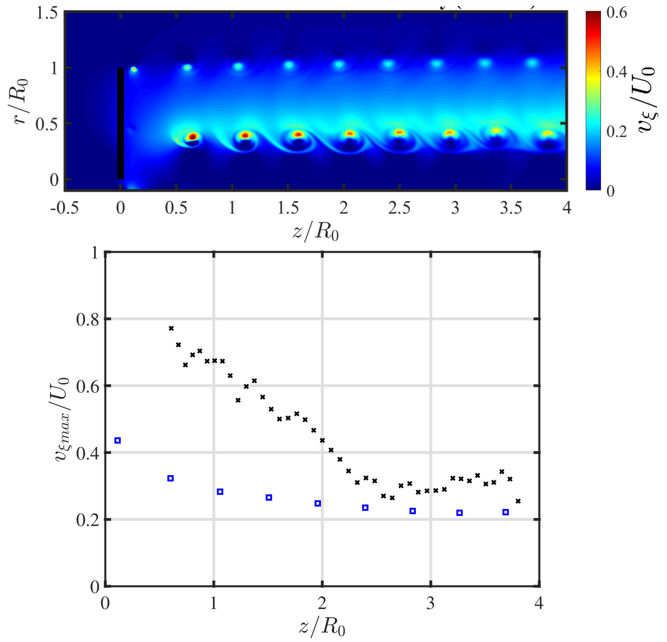

Figure 14: Top: Iso-velocity contours of the axial flow (out-of-plane) at $\lambda = 5.49$. Bottom: Maximum axial velocity in the core of the tip vortex as function of the the downstream position. Particle-mesh simulations [□] and estimation from experiments using dye [x].

The axial core flow, or out-of-plane velocity, is depicted in Figure 14. Since this velocity component was not captured using PIV during the experimental campaign, the maximum axial velocity is estimated by tracking in time the positions of the tip of the pattern of the dye entrained in the tip vortices [22]. A comparison with the simulated values of this maximum velocity shows a clear under-prediction by the numerical model near the rotor plane, while a better agreement is obtained further downstream ($z/R_0 \geq 2.3$). Similarly to the present investigation, the LES simulations in [19] for a single-blade configuration showed an even larger under-prediction of the maximum axial velocity in the core of the tip vortex. This difference with experiments was linked to the fact that the rotor blade boundary layers are not modeled in a lifting-line-based approach.

5.1.3. Mean velocity and vorticity fields

Figure 15 shows the time-averaged axial velocity field for tip speed ratios 5.49 and 8.04. From the figure, we can see how the wake expansion predicted by the solver is lower than the one observed in experiments. Increasing the tip speed ratio reduces the wake deficit in the mid span region as can be seen in the wake profile depicted in Figure 16 at five different downstream locations. The numerical results obtained at stations 8 and 10 R_0 indicate that the transition to a far-wake like profile has started for all cases. This can be appreciated by a smoothing of the sharp velocity variations related to the influence of the concentrated tip and root vortices.

The time-averaged azimuthal vorticity is shown in Figure 17. An overall good agreement is obtained between measurements and simulations. Besides the signature of the shaft boundary layer, the main difference here is that the root vortex strength in the simulations tends to decrease with increasing tip speed ratio, while the opposite occurs in the experimental data. Finally, note that for a tip speed ratio of 8.04, the experiments show a clear broadening of the mean tip vortex signature, which is related to the pairing phenomenon between consecutive vortices. In the numerical simulations, this effect appears slightly further downstream, outside of the area of interest depicted in the figure.

5.2. Asymmetric rotor

A comparison is conducted concerning the effect of rotor asymmetry on the behavior of the tip vortices in the wake.

5.2.1. Influence of the tip speed ratio

First, following Quaranta et al. [22], the effect of rotor tip speed ratio is investigated. For a constant radial offset of $\delta = 1.22$ mm (1.5% of R_0), four different tip speed ratios are again considered: $\lambda = 4.47, 5.49, 6.70$ and 8.04. Figure 18 shows iso-contours of vorticity magnitude from both numerical models alongside dye visualizations taken from the experiments for all four tip speed ratios. Qualitatively, the tip vortex behavior observed in the experiments is captured well by the simulations using both models until the wake breakdown begins in the experiments. Note that dye was not applied to the blade roots in the experiments, so the root vortices do not appear in the visualizations. The key feature of the asymmetric rotor wake is the occurrence of global pairing, or "leapfrogging", where vortex helices swap positions. The downstream position of this leapfrogging is well predicted by the simulations for all tip speed ratios.

The primary discrepancy between experiments and simulations is in the location where the vortices begin to break down. At low tip speed ratios, the spacing between adjacent vortices in the experiments is large enough so that breakdown is not observed in the field of view. However, increasing the tip speed ratio reduces the helix spacing, accelerating the onset of short-wave instabilities, which results from the enhanced interaction between neighboring vortices and leads to vortex breakdown [45]. This phenomenon is not observed in the simulations. In the particle-mesh simulations, vortices are seen to merge and continue to propagate stably downstream, particularly for the two higher tip speed ratios. It is possible that such amalgamation, as well as the absence of short-wave instabilities, is caused by the lack of sufficient mesh resolution to fully resolve the vortex core in the simulations. Increasing the resolution enough to accurately represent the vortex core is computationally very demanding, since the core radius is less than 2 mm. As shown for the unperturbed case above, with the current resolution of 1 mm, the vortex core size is overestimated, which causes the vortices to merge faster. In the hybrid-filament simulations, the maintained filament structure makes possible to clearly capture the downstream development of the tip and root vortices without the appearance of vortex merging and with a much coarser mesh resolution, in this case 4 mm. Note here that not accounting for the particle strength exchange plays in favour of the filament method, avoiding the appearance of small scale and high frequency flow instabilities.

A quantitative comparison of the leapfrogging location obtained from the simulations and experiments can be made. In the experiments, this location is identified using the time-averaged intensity of the dye visualization images, as described in [22]. With the simulation data, an analogous approach is employed using the mean vorticity fields, depicted for an example case in Figure 19. These vorticity fields show the deviation between the paths traveled by the vortices shed from the two blades at the mid-wake cross-section. The streamwise position of maximum radial separation between the two trajectories indicates the leapfrogging location z_{LF} [22]. The comparison with the experimental results is shown in Figure 20. The hybrid-filament simulations consistently over-estimate the leapfrogging distance across all tip speed ratios, but the particle-mesh simulations predict this distance more accurately. For the two higher tip speed ratios, the leapfrogging distance obtained from the simulations is slightly higher than that from the experiments, though within the estimated uncertainty. The simulations slightly under-estimate the leapfrogging distance at the two lower tip speed ratios.

5.2.2. Influence of the radial offset

The magnitude δ of the radial rotor offset, which leads to a difference in length of 2δ between the the two blades, was also varied in both the experiments and simulations. The iso-contours of vorticity magnitude from the simulations are compared with the dye visualizations from the experiments in Figure 21 for four different values of δ at a constant $\lambda = 5.52$. Once again, the tip vortex behavior is well-captured by the simulations. In these cases, tip vortex breakdown is not observed within the field of view of the experiments, nor in the simulations. Vortex merging occurs at the most downstream edge of the selected interval in the particle-mesh simulations, for the two cases with the largest perturbations. This merging is once again caused by the inability to resolve the vortex core, as discussed in the previous section.

The leapfrogging distance, defined in the same way as before, is compared between the simulations and experiments in Figure 22. For this series of measurements, the hybrid-filament simulations consistently predict the leapfrogging distance observed in the experiments with high accuracy. The particle-mesh simulations, on the other hand, consistently under-estimate the leapfrogging distance relative to the experiments.

Some of the differences between experiments and simulations concerning the leapfrogging can be related to the blockage effect of the water channel used in the experiments. As seen in Figure 6, the outer velocity in the experiments continues to increase downstream of the rotor plane, as the flow accelerates around the rotor and wake, leading to higher leapfrogging distances than expected for an infinite domain. Another source of discrepancy may be related to the difference in the vortex core size in both settings. A recent study by Abraham et al. [46] has found a (weak) dependence of the leapfrogging distance on the core size, with smaller cores resulting in faster leapfrogging.

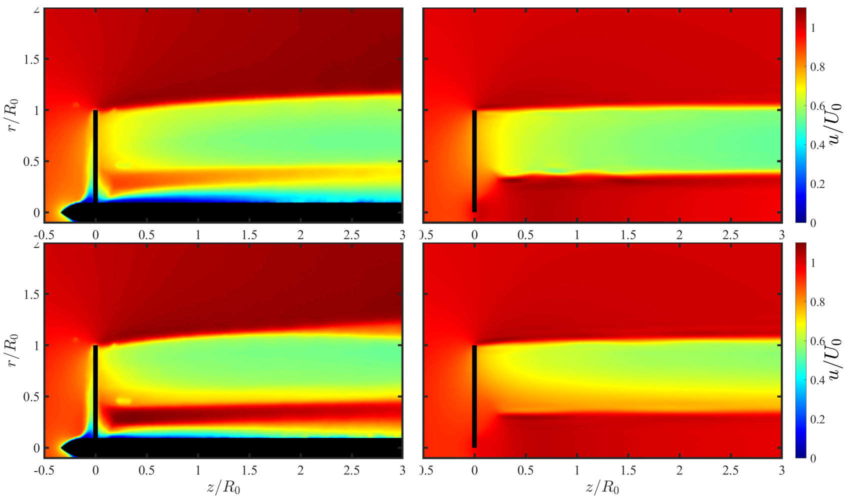

Figure 15: Mean non-dimensional axial velocity component for tip speed ratios of 5.49 (top) and 8.04 (bottom). Left: PIV measurements. Right: particle-mesh simulations.

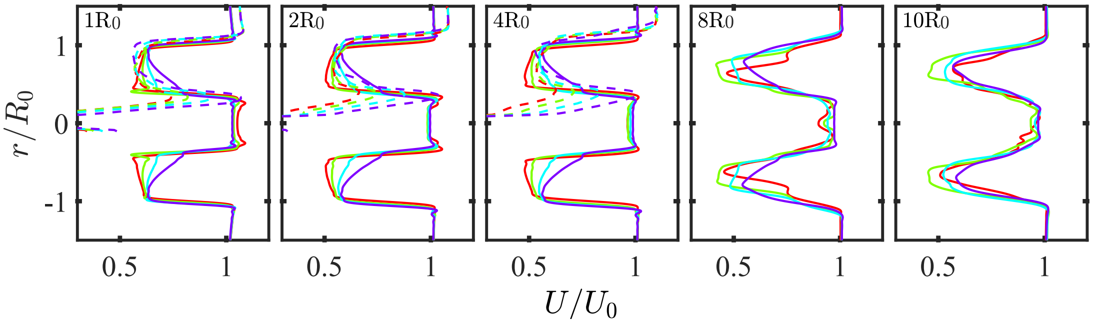

Figure 16: Streamwise velocity profiles at different downstream locations ($z = 1R_0$ to $10R_0$). Solid lines represent the particle-mesh simulations and experiments are depicted with dashed lines. $\lambda = 4.47$ [—], $\lambda = 5.49$ [—], $\lambda = 6.70$ [—] and $\lambda = 8.04$ [—]

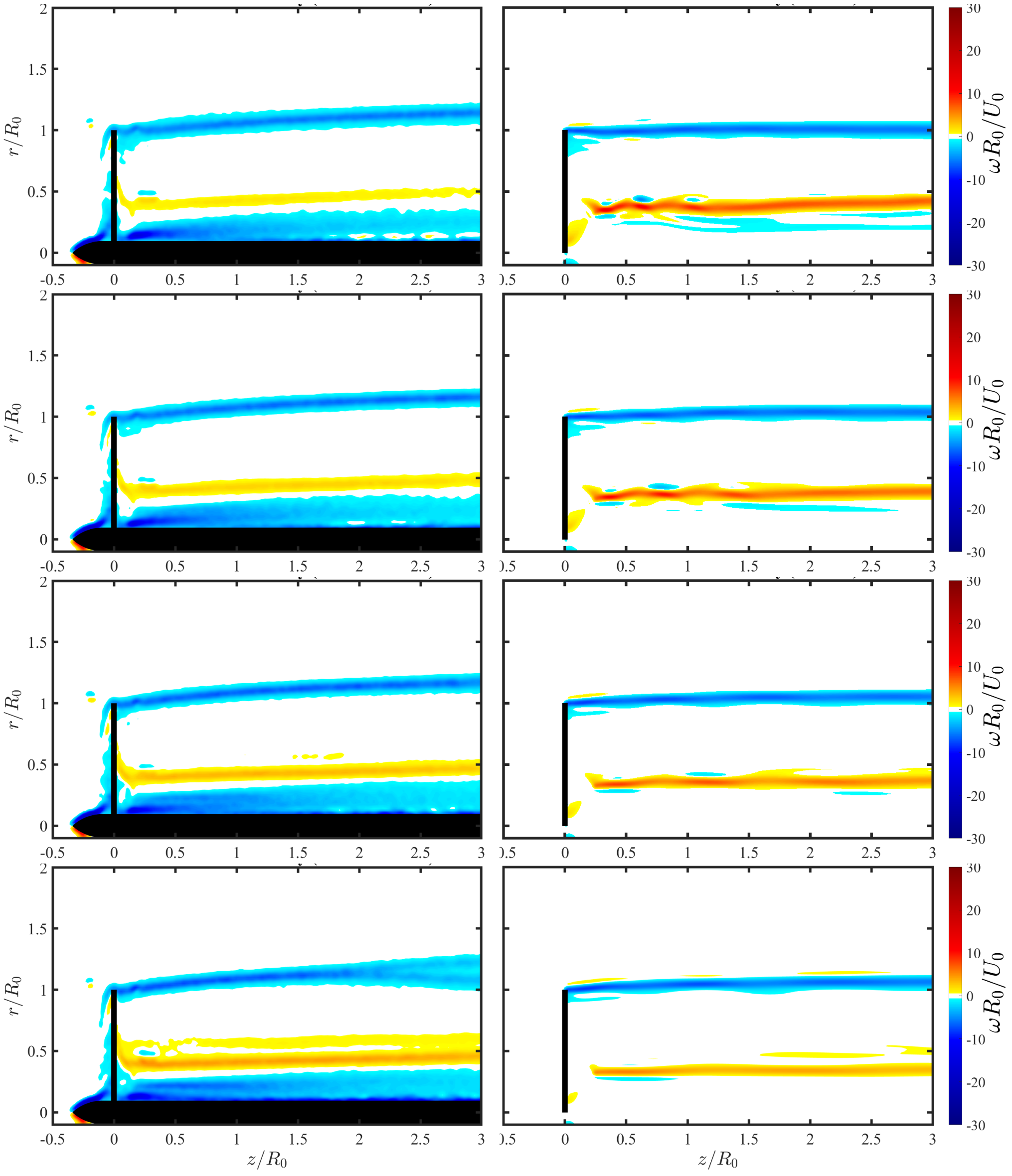

Figure 17: Mean non-dimensional azimuthal vorticity component, $\omega R_0/U_0$, for tip speed ratios $\lambda = 4.47$, 5.49, 6.70 and 8.04, from top to bottom. Left: PIV measurements. Right: particle-mesh simulations.

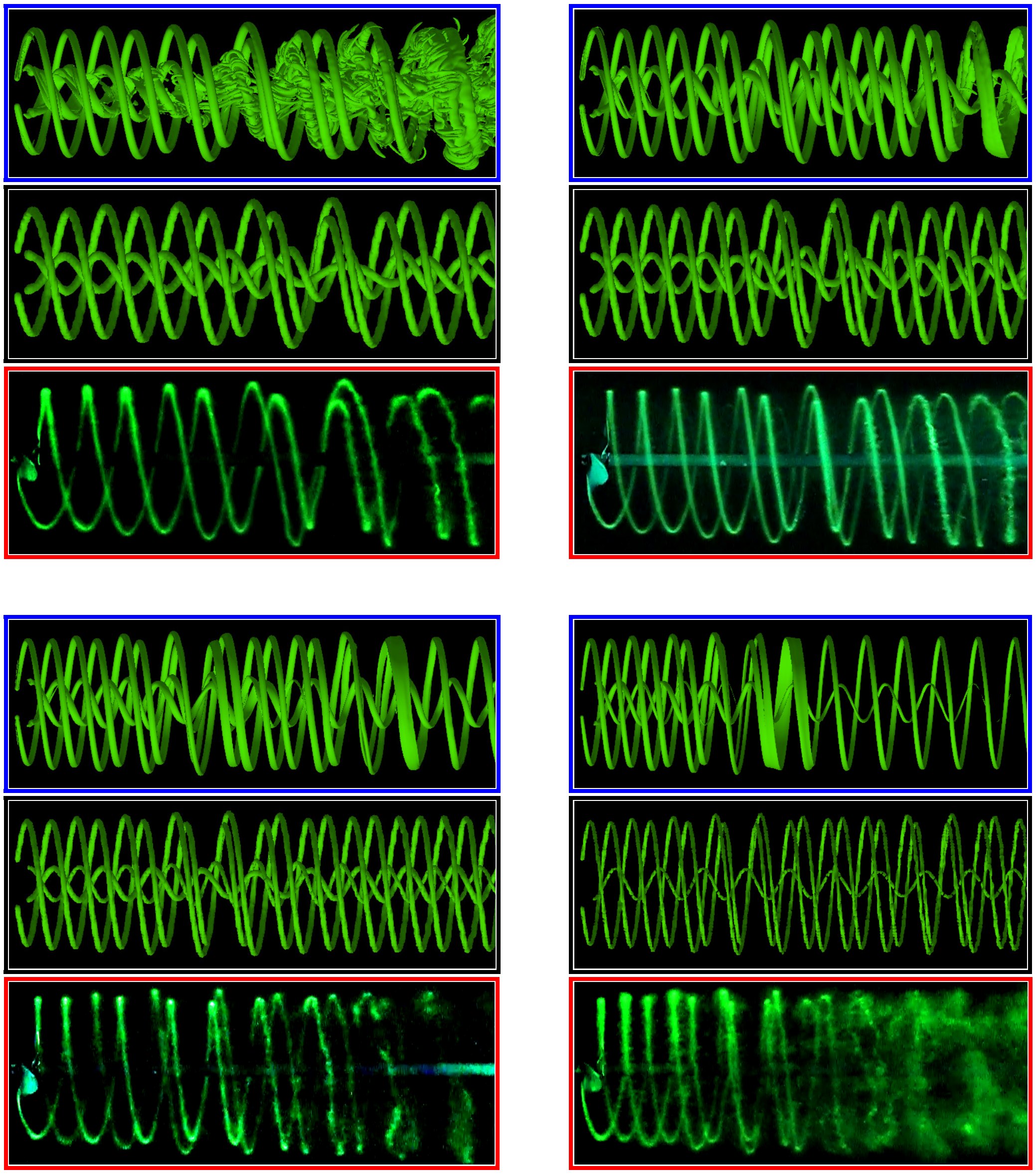

Figure 18: Wake structure of the asymmetric rotor (radial offset of 1.5% of R_0), for different tip speed ratios. From left to right and top to bottom: λ = 4.47, 5.49, 6.70 and 8.04. 3D iso-contours of vorticity magnitude from particle-mesh and hybrid-filament simulations are compared to experimental dye visualizations, framed in blue, black and red, respectively.

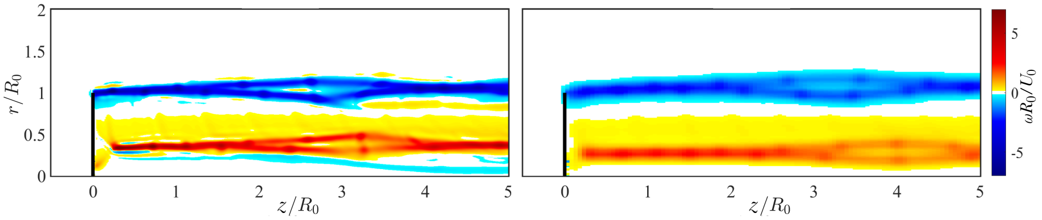

Figure 19: Mean azimuthal vorticity $\omega R_0/U_0$, for the case with $\lambda = 6.70$ and a radial blade offset of 1.22 mm. Left: high-resolution particle-mesh. Right: low-resolution hybrid-filament wake.

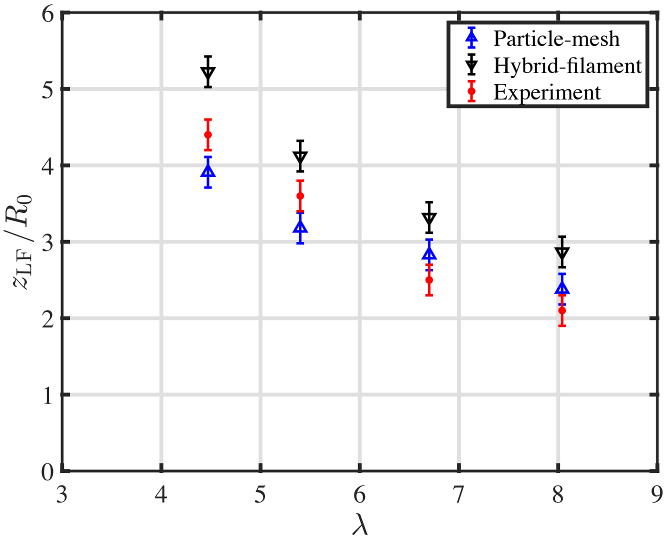

Figure 20: Leapfrogging location z_{LF} as function of tip speed ratio for a rotor configuration with a constant radial asymmetry (offset $\delta = 1.22$ mm, 1.5% of R_0). Comparison between experiment and simulations.

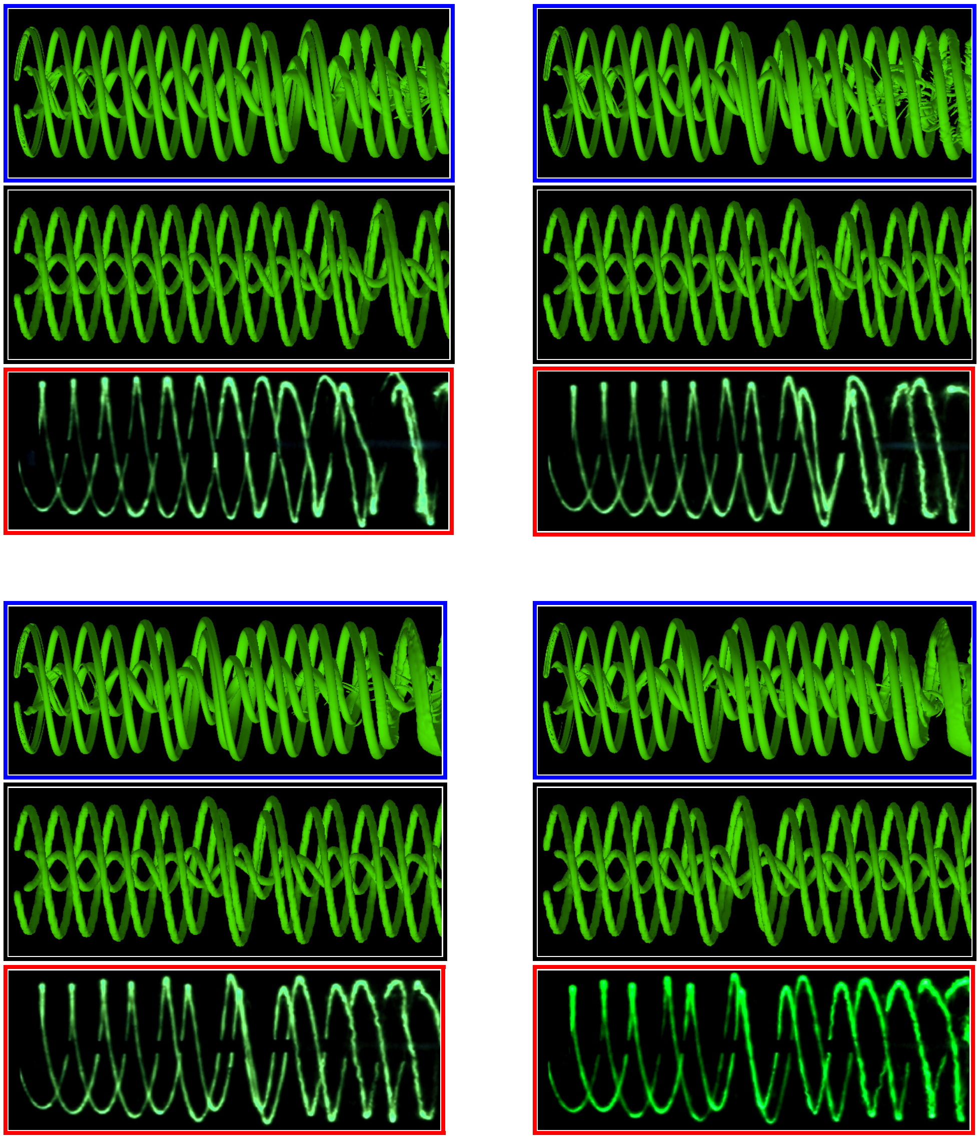

Figure 21: Wake structure of the asymmetric rotor for different radial offsets at constant tip speed ratio $\lambda = 5.52$. From left to right and top to bottom: $\delta = 0.2$, 0.7, 1.3 and 2.1 mm. 3D iso-contours of vorticity magnitude from particle-mesh and hybrid-filament simulations are compared to experimental dye visualizations, framed in blue, black and red, respectively.

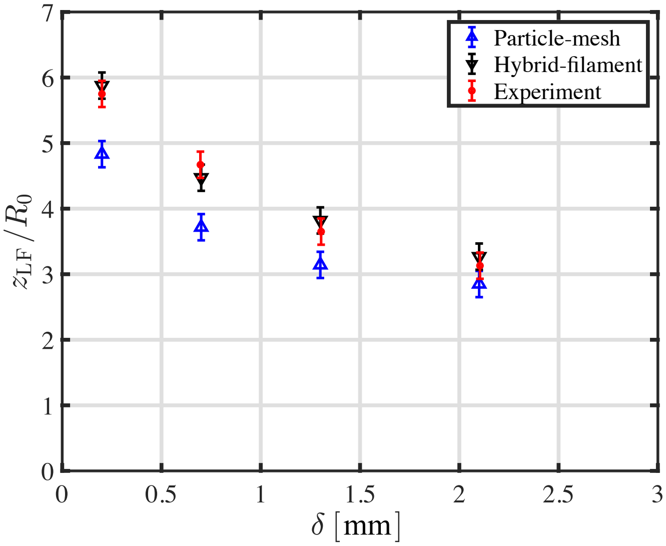

Figure 22: Leapfrogging location as function of the rotor radial offset, for $\lambda = 5.52$. Comparison between experiments and simulations.

6. Conclusion

The low power density of wind farms is mostly caused by the strong interaction between the turbines and the wakes generated by other upstream turbine rotors. Accelerating the wake recovery can therefore increase the available energy inside the wind farm, boosting its efficiency. In this study, we have carried out a very detailed validation of two different flow models implemented in the DTU vortex solver **MIRAS**. This work is intended to constitute a basis for future instability studies with this solver. Although limitations in the comparison between the numerical models and experiments, related to force coefficient uncertainty, flow blockage and numerical resolution, constitute a challenge, the overall agreement is more than satisfactory. A qualitative validation summary of the capabilities of both solvers to predict the different flow features of a rotor wake is shown in Table 3. In general, the lower-fidelity hybrid-particle method is able to successfully capture the elementary tip vortex characteristics in the near wake, such as vortex location and strength. However, a comparison with PIV measurements with a window that covers up to six tip vortices with a 0.135 cm vector resolution has shown that, in order to obtain a realistic picture of the flow, the particle-mesh method is needed. A significantly higher resolution in both experiments and numerics is necessary to accurately capture the core profile of the tip vortices. A new experimental campaign with a 0.008 cm vector resolution has been presented. Such fine resolution comes at the expense of a smaller measurement window, which can only capture a single tip vortex. In the numerical model, one cannot reduce the domain size without reducing the accuracy of the method. Therefore, due to computational resource availability, a minimum grid size of 0.05 cm has been used. With such resolution constraints, the simulations appear to predict a slightly larger core size, although the core growth rate is very similar to the theoretical one fitted to experiments. The particle-mesh solver predicts that the viscous core resulting from the roll-up process behind the blade approaches a Gaussian shape, while in the PIV measurements a core velocity profile with a slightly less pronounced outer slope has been found. Finally, regarding the leapfrogging location of the vortices in the wake of an asymmetric rotor, both solvers can capture the evolution of the underlying pairing instability fairly well. Regarding the computational time, the hybrid filament simulations with a resolution $\Delta = 0.4$ cm have been carried out in 32 cores during approximately 4 hours. The higher fidelity particle-mesh simulations with $\Delta = 0.1$

	Particle-mesh	**Hybrid-filament**
Vortex location	✓✓✓	✓✓✓
Vortex strength	✓✓✓	✓✓✓
Viscous core size	✓✓	✓
Viscous core profile	✓✓	✓
Viscous core growth	✓✓✓	✓
Instantaneous flow field	✓✓✓	✓
Mean flow field	✓✓✓	✓✓
Near wake profile	✓✓✓	✓
Far wake profile	✓✓✓	✓
Wake interaction	✓✓✓	✓
Leapfrogging location	✓✓✓	✓✓✓

Table 3: Qualitative comparison of the efficacy of the particle-mesh and hybrid-filament methods.

cm have been performed in 384 cores for about 12 hours. Finally, a single particle-mesh simulation with the very fine resolution of $\Delta = 0.05$ cm has been carried out in 800 cores during approximately 69 hours. In the future, the **MIRAS** solver will be used for the assessment of the impact of the radial blade perturbation on the far wake flow, focusing on its effect on turbines located downstream. Additionally, other types of geometrical perturbations will be studied, e.g. blade bending, winglets, flaps, etc.

CRediT authorship contribution statement

Néstor Ramos-García: Conceptualization, Methodology, Software, Investigation, Data curation, Writing – original draft, Writing – review & editing, Visualization, Project administration. **Aliza Abraham:** Conceptualization, Methodology, Investigation, Writing – review & editing. **Thomas Leweke:** Conceptualization, Methodology, Data curation, Writing – review & editing, Project administration, Funding acquisition. **Jens Nørkær Sørensen:** Writing – review & editing, Funding acquisition.

Declaration of competing interest

The authors declare that they have no known competing financial interests or personal relationships that could have appeared to influence the work reported in this paper.

Data availability

Data can be made available on request.

Acknowledgement

The authors would like to acknowledge the support from the Department of Wind Energy and Energy Systems of the Technical University of Denmark and the technology transfer company SATT Sud-Est, Marseille. Computations were performed on Sophia, a high performance computing cluster at Risø Campus, Technical University of Denmark.

References

[1] Smith G, Schlez W, Liddell A, Neubert A, Pena A. Advanced wake model for very closely spaced turbines. In: European Wind Energy Conference. 2006, Athens.

[2] Barthelmie RJ, Frandsen ST, Rathmann O, Hansen KS, Politis E, Prospathopoulos J, et al. Flow and wakes in large wind farms: Final report for UpWind WP8. Tech. Rep. Risø-R-1765(EN); Risø National Laboratory for Sustainable Energy, Technical University of Denmark; 2011. ISBN: 978-87-550-3878-3.

[3] Sørensen JN. Instability of helical tip vortices in rotor wakes. J Fluid Mech 2011;682:1–4. doi:`10.1017/jfm.2011.277`.

[4] Lee JCY, Fields MJ. An overview of wind-energy-production prediction bias, losses, and uncertainties. Wind Energ Sci 2021;6:311–65. doi:`10.5194/wes-6-311-2021`.

[5] Gebraad PMO, van Wingerden JW. A control-oriented dynamic model for wakes in wind plants. J Phys: Conf Ser 2014;524:012186. doi:`10.1088/1742-6596/524/1/012186`.

[6] Hulsman P, Andersen SJ, Göçmen T. Optimizing wind farm control through wake steering using surrogate models based on high-fidelity simulations. Wind Energ Sci 2020;5:309–29. doi:`10.5194/wes-5-309-2020`.

[7] Nemes A, Lo Jacono D, Blackburn HM, Sheridan J. Mutual inductance of two helical vortices. J Fluid Mech 2015;774:298–310. doi:`10.1017/jfm.2015.288`.

[8] Veers P, Dykes K, Lantz E, Barth S, Bottasso CL, Carlson O, et al. Grand challenges in the science of wind energy. Science 2019;366(6464):1–17. doi:`10.1126/science.aau2027`.

[9] Levy H, Forsdyke AG, Chapman S. The steady motion and stability of a helical vortex. Proc R Soc Lond A 1928;120(786):670–90. doi:`10.1098/rspa.1928.0174`.

[10] Widnall SE. The stability of a helical vortex filament. J Fluid Mech 1972;54:641–663. doi:`10.1017/S0022112072000928`.

[11] Leishman JG, Bhagwat MJ, Ananthan S. The vortex ring state as a spatially and temporally developing wake instability. J Am Helicopter Soc 2004;49:160–75. doi:`10.4050/JAHS.49.160`.

[12] Bhagwat MJ, Leishman JG. Stability analysis of helicopter rotor wakes in axial flight. J Am Helicopter Soc 2000;45:165–78. doi:`10.4050/JAHS.45.165`.

[13] Okulov VL, Sørensen JN. Stability of helical tip vortices in a rotor far wake. J Fluid Mech 2007;576:1–25. doi:`10.1017/S0022112006004228`.

[14] Joukowsky NE. Théorie tourbillonnaire de l'hélice propulsive. Paris: Gauthier-Villars; 1929.

[15] Vermeer LJ, Sørensen JN, Crespo A. Wind turbine wake aerodynamics. Prog Aerosp Sci 2003;39:467–510. doi:`https://doi.org/10.1016/S0376-0421(03)00078-2`.

[16] Walther JH, Guenot M, Machefaux E, Rasmussen JT, Chatelain P, Okulov VL, et al. A numerical study of the stability of helical vortices using vortex methods. J Phys: Conf Ser 2007;75:012034. doi:`10.1088/1742-6596/75/1/012034`.

[17] Ivanell S, Mikkelsen R, Sørensen JN, Henningson D. Stability analysis of the tip vortices of a wind turbine. Wind Energ 2010;13:705–15. doi:`10.1002/we.391`.

[18] Sarmast S, Dadfar R, Mikkelsen RF, Schlatter P, Ivanell S, Sørensen JN, et al. Mutual inductance instability of the tip vortices behind a wind turbine. J Fluid Mech 2014;755:705–731. doi:`10.1017/jfm.2014.326`.

[19] Ivanell S, Leweke T, Sarmast S, Quaranta HU, Mikkelsen RF, Sørensen JN. Comparison between experiments and Large-Eddy Simulations of tip spiral structure and geometry. J Phys: Conf Ser 2015;625:012018. doi:`10.1088/1742-6596/625/1/012018`.

[20] Quaranta HU, Bolnot H, Leweke T. Long-wave instability of a helical vortex. J Fluid Mech 2015;780:687–716. doi:`10.1017/jfm.2015.479`.

[21] Felli M, Camussi R, Di Felice F. Mechanisms of evolution of the propeller wake in the transition and far fields. J Fluid Mech 2011;682:5–53. doi:`10.1017/jfm.2011.150`.

[22] Quaranta HU, Brynjell-Rahkola M, Leweke T, Henningson DS. Local and global pairing instabilities of two interlaced helical vortices. J Fluid Mech 2019;863:927–955. doi:`10.1017/jfm.2018.904`.

[23] Ramos-García N, Sørensen JN, Shen WZ. Three-dimensional viscous-inviscid coupling method for wind turbine computations. Wind Energ 2016;19:67–93. doi:`10.1002/we.1821`.

[24] Sessarego M, Ramos-García N, Sørensen JN, Shen WZ. Development of an aeroelastic code based on three-dimensional viscous-inviscid method for wind turbine computations. Wind Energ 2017;20:1145–70. doi:`10.1002/we.2085`.

[25] Ramos-García N, Hejlesen MM, Sørensen JN, Walther JH. Hybrid vortex simulations of wind turbines using a three-dimensional viscous-inviscid panel method. Wind Energ 2017;20:1871–89. doi:`10.1002/we.2126`.

[26] Ramos-García N, Spietz HJ, Sørensen JN, Walther JH. Vortex simulations of wind turbines operating in atmospheric conditions using a prescribed velocity-vorticity boundary layer model. Wind Energ 2019;21:1216–31. doi:`10.1002/we.2225`.

[27] Hockney RW, Eastwood JW. Computer Simulation Using Particles. Boca Raton, FL: CRC Press; 1988. ISBN: 978-0852743928.

[28] Christiansen IP. Numerical simulation of hydrodynamics by the method of point vortices. J Comput Phys 1973;13:363–79. doi:`10.1016/0021-9991(73)90042-9`.

[29] Rasmussen JT. Particle methods in bluff body aerodynamics. Ph.D. thesis; Technical University of Denmark; 2011. ISBN: 978-87-90416-86-7.

[30] Hejlesen MM. A high order regularisation method for solving the Poisson equation and selected applications using vortex methods. Ph.D. thesis; Technical University of Denmark; 2016. ISBN: 978-87-7475-444-2.

[31] Hejlesen MM, Rasmussen JT, Chatelain P, Walther JH. A high order solver for the unbounded Poisson equation. J Comput Phys 2013;252:458–67. doi:`10.1016/j.jcp.2013.05.050`.

[32] Ramos-García N, Sessarego M, Horcas SG. Aero-hydro-servo-elastic coupling of a multi-body finite-element solver and a multi-fidelity vortex method. Wind Energ 2021;24:481–501. doi:`10.1002/we.2584`.

[33] Smagorinsky J. General circulation experiments with the primitive equations: I. The basic experiment. Mon Weather Rev 1963;91:99–164. doi:`10.1175/1520-0493(1963)091<0099:GCEWTP>2.3.CO;2`.

[34] Cocle R, Dufresne L, Winckelmans G. Investigation of multiscale subgrid models for les of instabilities and turbulence in wake vortex systems. In: Kassinos SC, Langer CA, Iaccarino G, Moin P, editors. Complex Effects in Large Eddy Simulations; vol. 56 of *Lecture Notes in Computational Science and Engineering*. Heidelberg: Springer; 2007, p. 141–159. doi:`10.1007/978-3-540-34234-2_11`.

[35] Selig MS, Guglielmo JJ, Broeren AP, Giguere P. Summary of Low-Speed Airfoil Data - Volume 1. Virginia Beach, VA: SoarTech Publications; 1995. ISBN: 0-9646747-1-8.

[36] Meunier P, Leweke T. Analysis and optimization of the error caused by high velocity gradients in piv. Exp Fluids 2003;35:408–21.

[37] Drela M. XFOIL: An analysis and design system for low Reynolds number airfoils. In: Mueller TJ, editor. Low Reynolds Number Aerodynamics; vol. 54 of *Lecture Notes in Engineering*. Berlin: Springer; 1989, p. 1–12. doi:`10.1007/978-3-642-84010-4_1`.

[38] Ramaswamy R, Bourantas G, Jülicher F, Sbalzarini IF. A hybrid particle-mesh method for incompressible active polar viscous gels. Journal of Computational Physics 2015;291:334–61. URL: `https://www.sciencedirect.com/science/article/pii/S0021999115001412`. doi:`https://doi.org/10.1016/j.jcp.2015.03.007`.

[39] Caprace DG, Winckelmans G, Chatelain P. An immersed lifting and dragging line model for the vortex particle-mesh method. Theoretical and Computational Fluid Dynamics 2020;34:21–48. doi:`10.1007/s00162-019-00510-1`.

[40] Spietz H, Mekanik DTUD, for Applied Mathematics DC, Mechanics . A Vortex-particle Mesh Method for Large Eddy Simulation of Bluff Body Aerodynamics: PhD Thesis. DCAMM special report; DTU Mechanical Engineering; 2018. ISBN 9788774755364. URL: `https://books.google.dk/books?id=sYTgxQEACAAJ`.

[41] Snel H, Schepers J, Montgomerie B. The mexico project (model experiments in controlled conditions): The database and first results of data processing and interpretation. In: Journal of Physics: Conference Series; vol. 75. IOP Publishing; 2007, p. 012014.

[42] Scully MP. Computation of helicopter rotor wake geometry and its influence on rotor harmonic airloads. Ph.D. thesis; Massachusetts Institute of Technology; 1975. URL: `https://dspace.mit.edu/handle/1721.1/64826`.

[43] Kirde K. Untersuchungen über die zeitliche Weiterentwicklung eines Wirbels mit vorgegebener Anfangsverteilung. Ing-Arch 1962;31:385–404. doi:`10.1007/BF00536491`.

[44] Moore DW, Saffman PG. Axial flow in laminar trailing vortices. Proc R Soc Lond A 1973;333:491–508. doi:`10.1098/rspa.1973.0075`.

[45] Leweke T, Quaranta HU, Bolnot H, Blanco-Rodríguez FJ, Le Dizès S. Long-and short-wave instabilities in helical vortices. J Phys: Conf Ser 2014;524:012154. doi:`10.1088/1742-6596/524/1/012154`.

[46] Abraham A, Castillo-Castellanos A, Leweke T. Simplified model for helical vortex dynamics in the wake of an asymmetric rotor. Flow 2022; submitted.